LANGMUIR

pubs.acs.org/Langmuir Article

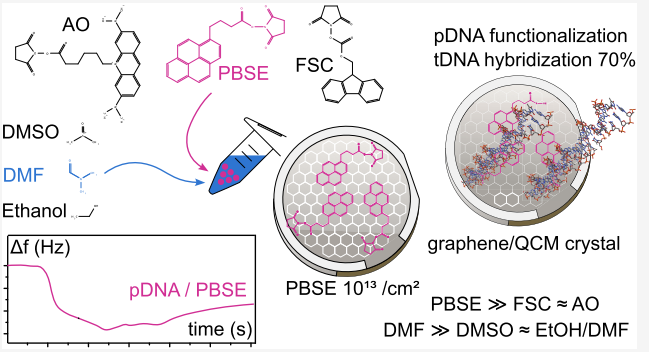
Tailoring DNA Surface Interactions on Single-Layer Graphene: Comparative Analysis of Pyrene, Acridine, and Fluorenyl Methyl Linkers

Telma Domingues, Chun-Da Liao, Marta Prado, M. Fátima Cerqueira, Dmitri Y. Petrovykh, Pedro Alpuim, Jérôme Borme,* and Joana Rafaela Guerreiro*

Cite This: *Langmuir* 2025, 41, 263−273 Read Online

ACCESS | Metrics & More | Article Recommendations | Supporting Information

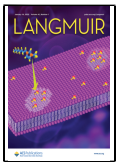
ABSTRACT: This study investigates the effect of different linkers and solvents on the immobilization of DNA probes on graphene surfaces, which are crucial for developing high-performance biosensors. Quartz crystal microbalance with dissipation (QCM-D) measurements were used to characterize in situ and real-time the immobilization of ssDNA and hybridization efficiency on model graphene surfaces. The DNA probes immobilization kinetics and thermodynamics were systematically investigated for all the pairings between three bifunctional linkers—1-pyrenebutyric acid succinimidyl ester (PBSE), Fluorenylmethylsuccinimidyl carbonate (FSC), and Acridine Orange (AO) succinimidyl ester—and three organic solvents (DMF, DMSO, and 10% DMF/ethanol). The linker's spatial orientation and effective surface modification for DNA probe attachment were also evaluated based on footprints and DNA probe surface coverage. Graphene surfaces functionalized with PBSE in DMF achieved the highest DNA probe surface density (up to 1.31×10^{13} molecules cm^{-2}) and fastest kinetic, p values above 4, and hybridization efficiencies of at least 70%, with 20 to 30% of ssDNA directly adsorbed nonspecifically on the functionalized graphene surface, which has significant implications for the design of sensitive biosensors. The efficiency of the ethanolamine-NHS blocking reaction was estimated to be 80%. The surface packing density of the linker was estimated at 25% of the entire surface coverage for PBSE, and about 22 and 13% for AO and FSC, respectively. Overall, the surface coverage achieved for probe DNA was in the same order of magnitude as that obtained on flat gold surfaces ($\geq 10^{13}$ molecules cm^{-2}), typically used in biosensors. These findings highlight the importance of the selected conditions for graphene surface modification to achieve high DNA probe surface density on graphene materials. These results underscore the critical role of interface engineering in achieving target functional outcomes in biosensing technology.



INTRODUCTION

Most fundamental biochemical events in the human body rely on the binding kinetics and thermodynamics of interactions between DNA, RNA, proteins, and small ligands, which are the basis for developing specific biosensors. DNA molecules provide exceptional specificity, versatility, and sensitivity, establishing them as a fundamental building block in the design of advanced biosensors with wide-ranging applications.[1,2] The biosensing research field has been focusing on mimicking natural biochemical mechanisms to deeply understand and provide new insights in areas ranging from detecting disease biomarkers to exploring DNA−DNA interactions[3−8] which are crucial for application in diagnostics, environmental monitoring, food control, and many other applications.[9] DNA-based biosensors exploit the unique benefit of a robust deterministic relationship between DNA sequences and biorecognition specificity and reliability.[10,11] Advancements in the fast and inexpensive synthesis of oligonucleotides combined with the rapid hybridization of complementary DNA strands, make synthetic oligonucleotides highly practical as recognition elements in biosensors.[12,13] The ability to control DNA spatial orientation through surface functionalization is critical to optimize DNA−DNA interaction at solid surfaces, a key factor in achieving excellent analytical performance of biosensor microarrays.[14] Typically, in DNA-based biosensors a short single-stranded DNA (ssDNA) with a specific sequence (DNA probe) is immobilized onto a surface for further hybridization with the complementary ssDNA

Received: September 3, 2024
Revised: December 12, 2024
Accepted: December 16, 2024
Published: December 23, 2024



ACS Publications © 2024 American Chemical Society

https://doi.org/10.1021/acs.langmuir.4c03420
Langmuir 2025, 41, 263−273

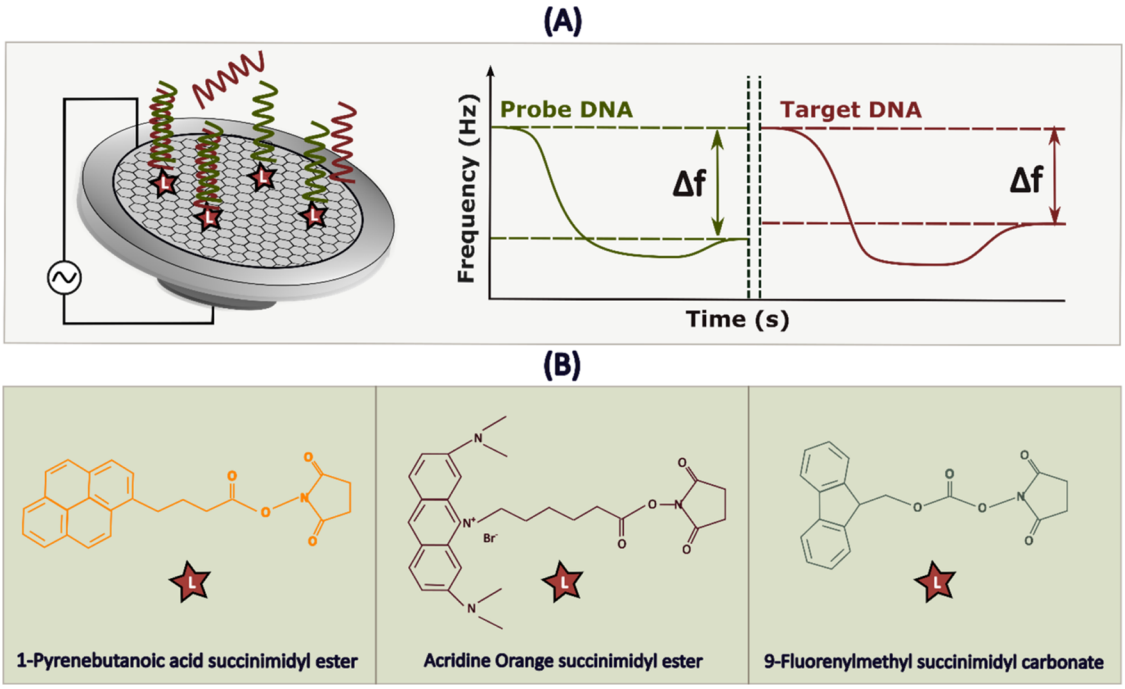


Figure 1. (A) QCM-D Setup. Left: A schematic diagram of QCM-D and the SiO_2 quartz crystal with graphene on top, functionalized with different linkers, and single-strand DNA is attached and ready to form double-stranded DNA. Right: Typical QCM measurements illustrate the changes in the resonance frequency, Δf, after probe immobilization and target DNA detection. (B) Chemical structure of the linkers studied in this work. Left: 1-pyrenebutyric acid succinimidyl ester (PBSE); Center: acridine orange succinimidyl ester (AO). Right: fluorenylmethyl succinimidyl carbonate (FSC).

target (in solution).[15,16] Gold surfaces remain a popular choice for DNA immobilization, due to their inert properties, biocompatibility, conductivity, and ease of chemical modification with diverse functional groups through the self-assembly of alkanethiols.[17,18] The thiol adsorption mechanism and self-assembled monolayers' formation on gold are already deeply understood.[19,20] Likewise, the thiol-modified DNA molecules bind to gold through thiol single-atom attachment, showing good stability, reproducibility, and high surface densities ($\geq 10^{13}$ molecules/cm^2). However, with the emergence of two-dimensional (2D) materials, alternative transducers for biosensing applications are being explored offering potential advantages. Graphene-based biosensors have been attracting growing attention due to their extremely high sensitivity based on graphene's unique electronic properties and high chemical and mechanical stability.[21,22] Graphene is a single layer of carbon atoms in a perfect honeycomb lattice, with remarkable transducing sensitivity,[23] sizable specific surface area,[24] biocompatibility,[25] decreased manufacturing cost,[26] and high signal-to-noise features.[27−30] These features position graphene as a leading material for next-generation biosensing technologies.

Graphene-based DNA biosensing critically depends on surface functionalization, which can be achieved by covalent or noncovalent immobilization.[31−33] Covalent surface functionalization is commonly applied to graphene-derived materials, such as graphene oxide, due to its characteristically multiple oxygen functional groups and their reactivity for surface modification.[34] Covalent functionalization of pristine graphene can be achieved without compromising the graphene quality and biosensor analytical performance, as we have shown elsewhere.[35] However, expensive machinery is required, which can complicate the industrial upscaling of these methods. In contrast, noncovalent functionalization is advantageous as it is easy to perform and preserves the intrinsic properties of graphene while offering a strong attachment for DNA probes. Typically, graphene-based DNA sensors exploit the graphene interaction with the negatively charged network of the DNA phosphate backbone or its aromatic nitrogenous bases.[36] DNA can also be immobilized on the graphene surface by physical adsorption through electrostatic van der Waals interactions or by covalently binding to (hetero)bifunctional linkers that anchor to graphene via $\pi-\pi$ or hydrophobicity stacking.[37−39] Short DNA sequences, DNA composition, and low pH favor their rapid adsorption to graphene. Nevertheless, the affinity of DNA bases may differ between graphene and other materials, such as graphene oxide, due to the distinct surface properties of each material.[40] While a consensus suggests the order G > A > C > T for adsorption onto graphene, discrepancies exist regarding the relative affinity between C and T.[41−43] Despite the importance of these interactions, the mechanisms underlying the oriented attachment of DNA sequences using (hetero)bifunctional linkers have been neglected, considering that only an indirect measure of hybridization efficiency is commonly assessed.

Several ligands have been employed in noncovalent graphene functionalization, primarily derived from aromatic organic molecules, such as pyrene-butyric acid,[44−46] tryptamine,[47] and 1-aminopyrene[48] often without further surface characterization. Among various bifunctional linkers, pyrene derivatives, such as the 1-pyrene butyric succinimidyl ester (PBSE), are the most commonly used for graphene functionalization[49] inspired by their successful use in carbon nanotube-based biosensors. PBSE relies on the van der Waals interaction between the pyrene group and graphene, yet studies exploring linkers based on other conjugated groups,

https://doi.org/10.1021/acs.langmuir.4c03420
Langmuir 2025, 41, 263−273

such as those derived from acridine and fluorenyl methylcarbamate, are limited.[50]

Therefore, there is a clear need to enhance and understand graphene functionalization by investigating the mechanism of probe attachment, the kinetics of DNA immobilization, and the influence of linkers and solvent selection on the DNA surface coverage and binding stability. These new insights are fundamental for improving DNA sensing on graphene, as the DNA probe surface coverage strongly influences the hybridization efficiency and kinetics. Techniques such as surface plasmon resonance (SPR),[51] X-ray photoelectron spectroscopy (XPS),[24,52] and quartz crystal microbalance with dissipation monitoring (QCM-D),[53] allow the label-free monitoring of the kinetics and surface coverage of DNA probe immobilization.[54]

Here, we systematically investigate DNA immobilization and surface density onto pristine graphene using three van der Waals (hetero)bifunctional linkers with different footprints. We also assess the impact of the linker's solvent on the immobilization process. Taking advantage of the versatility and high sensitivity of QCM-D, we measure the molecular density coverage of the graphene surfaces for each linker and evaluate its effect on the DNA probe immobilization. Real-time monitoring of DNA probe-target hybridization allowed the quantification of DNA probe density on graphene, which was further assessed using graphene multitransistor biosensing chips functionalized with ssDNA probes immobilized by one of the three linkers and measuring the sensor's signal at saturation after DNA hybridization completion (Figure 1A). The process is repeated for the other two linkers.

MATERIALS AND METHODS

Chemicals and Biomolecules. 1-pyrenebutyric acid succinimidyl ester (PBSE, CAS 114932−60−4, $C_{24}H_{19}NO_4$, M = 385.41 g/mol), *N*,*N*-dimethylformamide (DMF), ethanol (EtOH), dimethyl sulfoxide (DMSO), ethylenediaminetetraacetic acid (EDTA), Alconox detergent, sodium hydroxide, calcium chloride, tris(hydroxymethyl)-aminomethane (Tris), Tris-EDTA buffer (TE), and ethanolamine (ETA) were purchased from Sigma-Aldrich. Hexamethyldisilazane (HMDS) was purchased from Technic. Fluorenylmethylsuccinimidyl carbonate (FSC, CAS 82911−69−1, $C_{19}H_{15}NO_5$, M = 337.34 g/mol; also referred to as Fmoc-OSu) was purchased from Alfa Aesar (catalog item A13143). Acridine orange succinimidyl ester (AO, $C_{27}H_{33}BrN_4O_4$, M = 577.49 g/mol) was purchased from Biotium (catalog item 40074). Probe DNA sequence (pDNA) 3′C6-amino modification (5′- TCA TAA CCG GCG AAA GGC TGA AGC T-3′, T_m = 77.5 °C, M = 7909 g/mol), the complementary target DNA (tDNA) (5′-AGC TTC AGC CTT TCG CCG GTT ATG A-3′, T_m = 80.4 °C, M = 7624 g/mol), from*Vitis vinifera* (wine grape), were synthesized by Metabion International AG, Martinsried, Germany.

Measurements with Quartz Crystal Microbalance with Dissipation (QCM-D). QCM crystals coated with silicon dioxide (QSX 335, Biolin scientific: SiO_2 50 nm with adhesion layer Ti 100 nm) were used as substrates for transferring CVD-grown graphene (2 × 2 cm^2). When used for the first time, the crystals were rinsed with ethanol and MQ, dried in nitrogen, cleaned in oxygen plasma for 2 min, and stored in MQ until graphene transfer. When reused, the crystals were cleaned with 1% Alconox aqueous solution at 60 °C for 1 h, followed by exposure to oxygen plasma (Gigabatch 360M, PVA Tepla, 500 sccm O_2, 100 sccm Ar, 5 Torr, 300 W) for 5 min. After that, the surface of the crystal was treated by HMDS in a vapor priming oven (310-TA, YES Engineering, 6 Torr, 150 °C, 300 s) to increase the graphene adhesion to the silicon dioxide that covers the QCM crystal surface. Details in the Supporting Information, Figures S1 and S2.

QCM-D experiments were conducted in a QSense E1 system (Biolin Scientific) where all the overtones were recorded simultaneously (3rd, 5th, 7th, 11th, and 13th). Before starting QCM-D experiments the crystals were verified as detailed in Supporting Information, Figure S3. A peristaltic pump controlled the flow rate. All measurements were performed at a temperature of 21 °C.

Surface Functionalization and DNA Probe Immobilization. Graphene surface functionalization was performed using three heterobifunctional linkers, PBSE, FSC, and AO succinimidyl ester (Figure 1B). Graphene-transferred crystals were incubated with a 100 μL droplet of each linker at 10 mM concentration, and placed in a humid chamber for 2 h, outside the QCM chamber. After incubation, the crystals were rinsed with the solvents used to prepare the linkers and then transferred to the QCM chamber. For pDNA immobilization, a running buffer of 0.99 M $CaCl_2$-TE (matched to the buffer concentration in the 1 μM pDNA solution) was injected at a flow rate of 60 μL/min until a stable baseline. Then, 1 mL of 1 μM pDNA solution (prepared by diluting 10 μL of 100 μM pDNA in 990 μL of 1 M CaC_2-TE) was injected for approximately 12 min, followed by recirculation, given the limited volume of the DNA solution. The pDNA was allowed to interact with the surface under continuous flow for 45 min. The surface was then rinsed with the DNA-matched running buffer until a plateau was reached, indicating the removal of nonspecifically bound DNA probes. A baseline was considered stable for frequency drifts within the 0.15−0.5 Hz range. Blocking of unreacted ester groups at the graphene surface was performed by incubating the crystal, outside the QCM chamber, for 30 min with aqueous 100 mM ethanolamine at pH 8.5. After the blocking, the surface was rinsed with water and immediately placed back inside the QCM chamber for hybridization experiments.

DNA Hybridization Experiments. Hybridization experiments were carried out by introducing the tDNA sequence complementary to the probe sequence (pDNA) immobilized on the graphene surface at a temperature of 21 °C. The measurements began by introducing the DNA matching buffer until a stable baseline was reached. Next, 1 mL of 1 μM tDNA (prepared by diluting 10 μL of 100 μM tDNA in 990 μL of 1 M $CaCl_2$-TE) was introduced into the system at a flow rate of 60 μL/min. Target recirculation started after ca. 8 min, and was allowed to continue for 45 min to facilitate hybridization. Subsequently, DNA-matched running buffer was pumped through the chamber to remove nonspecifically bound tDNAs. The QCM signals from DNA hybridization were quantified using three additional controls: (i) PBSE/pDNA/ETA/pDNA; (ii) PBSE/ETA/pDNA; and (iii) PBSE/ETA/tDNA. These controls were processed using the same solutions and procedures for surface functionalization, ester blocking, and DNA interaction.

RESULTS

Preparation of QCM Sensors. The quality of the graphene single-layer produced was evaluated by comparing optical images of the quartz crystal before and after graphene transfer. These images showed no evidence of cracks and discontinuities in the graphene layer across several square millimeters (Figure S4A−C). Analysis by Raman spectroscopy (Figure S5) and of the optical images (Figure S4D,E) indicates that single-layer graphene represents 79.2% of the graphene sample.

As expected, the Raman spectra of the graphene samples show the G-band at ≈1580 cm^{-1}, characteristic of the graphitic lattice vibration mode, and the 2D band at ≈2700 cm^{-1}, which corresponds to a second-order Raman process involving two phonons close to the zone boundary at the K point. Besides these two modes, the Raman spectra also show, although with lower intensity, the disorder-induced phonon mode D band at ≈1350 cm^{-1}. From the relative intensities of these modes, it is possible to differentiate between graphene single-layer and multilayer (I_{2D}/I_G) and assess the crystallographic quality of the graphene layer (I_D/I_G). The graphene on the QCM crystal (green line) presents an I_{2D}/I_G of 1.5, and the defects are

https://doi.org/10.1021/acs.langmuir.4c03420
Langmuir 2025, 41, 263−273

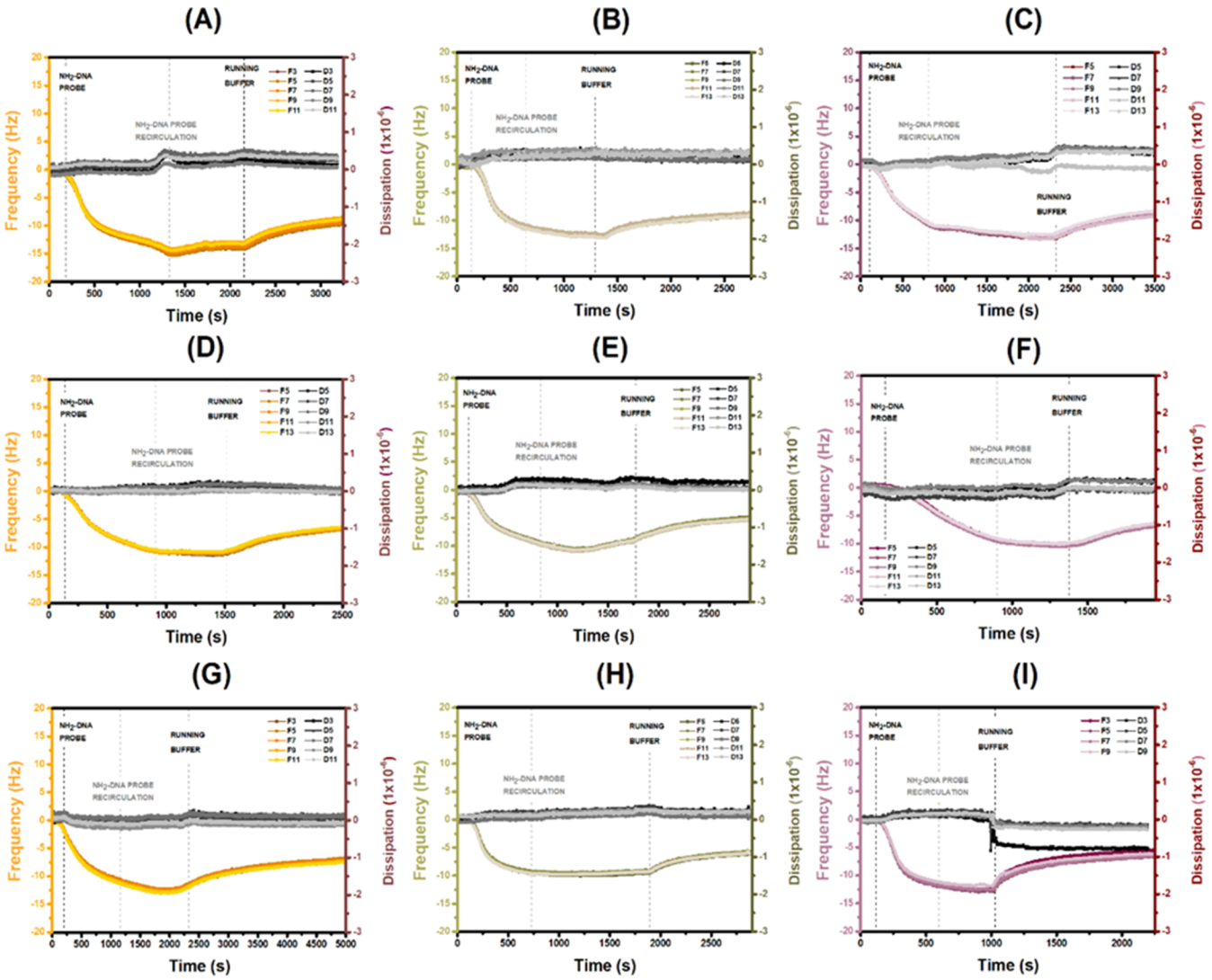


Figure 2. Frequency (left axis) and dissipation (right axis) change vs time response for probe immobilization with different linkers dissolved in different solvents. (A) Linker PBSE dissolved in DMF; (B) linker FSC dissolved in DMF; (C) linker AO dissolved in DMF; (D) linker PBSE dissolved in DMSO; (E) linker FSC dissolved in DMSO; (F) linker AO dissolved in DMSO; (G) linker PBSE dissolved in 10% DMF/EtOH; (H) linker FSC dissolved in 10% DMF/EtOH; (I) linker AO dissolved in 10% DMF/EtOH.

residual (I_D/I_G = 0.24), indicating a single-layer graphene with high crystalline quality[55] (Figure S5).

Surface Functionalization Experiments. This study systematically compared three heterobifunctional linkers, selected from the literature:[49,50] the PBSE, FSC, and AO, Figure 1B, for immobilizing ssDNA probes onto graphene surfaces. Benzene rings are expected to interact with graphene via $\pi-\pi$ interactions while reactive NHS ester groups undergo a nucleophilic substitution when exposed to primary amines, such as those in the amine-modified DNA probes (pDNA). The functionalization of graphene with the three linkers was also performed in three different solvents, DMF, DMSO, and ethanol combined with DMF. The DMF was chosen for its compatibility with carbon materials, as it is well-known for dissolving single-wall carbon nanotubes[56,57] and suspensions of graphite powders and oxides.[58] QCM-D measures precise changes in adsorbed mass and viscoelastic properties of adsorbed material[59] and was used in this study to monitor the immobilization and kinetics of pDNA by covalent binding to the linkers with different solvents, yielding the resulting surface density of pDNA immobilization.

Figure 2 displays the QCM-D frequency shift and dissipation signal as a function of time for the linkers and solvent combinations (additional details in Figure S6). In Figure 2A–I, three consecutive time points are marked with gray dashed vertical lines, corresponding to the injection of pDNA, recirculation of pDNA, and injection of the running buffer. When the amine-modified DNA probes covalently bind to the very reactive NHS esters at the graphene surface, a decrease in frequency is observed, simultaneously with a small energy dissipation (dark gray lines in Figure 2A–I). The pDNA recirculation slightly disturbs the flow equilibrium, promoting some DNA removal with immobilization kinetics slowing down until a stable frequency. The last step of running buffer enables the wash of nonreacted pDNA from the surface. The observed negative shift reflects an increase in mass on the QCM crystal due to the specific attachment of the pDNA molecules to the surface. Conversely, pDNA immobilization did not produce a significant change in dissipation; the

https://doi.org/10.1021/acs.langmuir.4c03420
Langmuir 2025, 41, 263−273

Table 1. pDNA-on-Graphene Density Calculated for Each Linker/Solvent Pair Based on QCM-D Frequency-Shift Measurements (Δf)

solvents	parameters[a]	PBSE	AO	FSC
DMF	Δf (Hz)	-9.11 ± 0.31	-8.43 ± 0.34	-7.36 ± 0.16
	ΔD (1×10^{-6})	0.27 ± 0.13	0.23 ± 0.11	0.14 ± 0.08
	density (molecules/cm^2)	$1.27 \pm 0.04 \times 10^{13}$	$1.18 \pm 0.05 \times 10^{13}$	$1.03 \pm 0.07 \times 10^{13}$
DMSO	Δf (Hz)	-7.58 ± 0.12	-6.59 ± 0.28	-5.95 ± 0.11
	ΔD (1×10^{-6})	0.15 ± 0.09	0.08 ± 0.04	0.19 ± 0.11
	density (molecules/cm^2)	$1.06 \pm 0.02 \times 10^{13}$	$9.22 \pm 0.93 \times 10^{12}$	$8.32 \pm 0.17 \times 10^{12}$
10% DMF/EtOH	Δf (Hz)	-6.83 ± 0.17	-6.11 ± 0.29	-6.05 ± 0.17
	ΔD (1×10^{-6})	0.23 ± 0.12	0.11 ± 0.06	0.11 ± 0.05
	density (molecules/cm^2)	$9.55 \pm 0.04 \times 10^{12}$	$8.55 \pm 0.16 \times 10^{12}$	$8.46 \pm 0.30 \times 10^{12}$

[a]Values based on the average of all QCM-D overtones except the 1st.

Table 2. Theoretical and Indirect Experimental Linker Densities for the Three Linkers[a]

	theoretical (densest regular packing)			observed			comparison
linker	footprint (nm^2)	linker geometrical density (molecules/cm^2)	intermolecular spacing (nm)	footprint (nm^2)	pDNA density (DMF) (molecules/cm^2)[b]	intermolecular spacing (nm)	coverage (density ratio) (%)
PBSE	**1.93**	5.18×10^{13}	2.11	7.87	**$1.27 \pm 0.04 \times 10^{13}$**	4.26	24.5
AO	**1.85**	5.40×10^{13}	2.07	8.47	**$1.18 \pm 0.05 \times 10^{13}$**	4.42	21.9
FSC	**1.29**	7.75×10^{13}	1.72	9.71	**$1.03 \pm 0.07 \times 10^{13}$**	4.74	13.3

[a]The theoretical footprint (in nm^2) and the observed density calculated from the saturated pDNA concentration (Table 1), highlighted in bold, are primary data from which the others were derived. The theoretical geometrical density is inversely proportional to the footprint area; the average intermolecular spacing is computed from the density assuming a densely-packed surface following a law of triangular networks $\rho = 4/(a2\sqrt{3})$; the coverage is expressed as the ratio between the observed density and the density of the closet packing. The observed density for DMF is the largest within the 3 solvents. [b]Calculated from QCM-D measurements. Values based on the average of all QCM-D overtones except the 1st.

magnitude in the order of 10^{-7} suggests a minimal change in the viscoelastic properties of the molecular biointerface, indicating that the pDNA is relatively rigid.

We calculated the surface density of pDNA immobilized on graphene for all linker-solvent pairs with the correction of 1.5% on the molecular density due to the amide bond formation, and NHS release for each pDNA strand added to the surface (details in the Supporting Information). The results are presented in Table 1. The main differences among the linkers structures, Figure 1B, are their footprint (pyrene, benzene rings with a pyridine, and a fluorene group) and the vertical distance to the reactive amine. For all three linkers, DMF is the solvent that consistently resulted in the highest pDNA density, within 33 to 39%, while the mixture of 10% DMF/EtOH led to the lowest pDNA density.

When comparing the use of the three linkers, independently of the solvent used, pDNA density was always highest with PBSE, intermediate with AO, and lowest with FSC. The difference in density between the linkers ranged from 12 to 27%, depending on the solvent. PBSE, the linker with the larger aromatic system, achieved the highest immobilization, which may be attributed to stronger $\pi-\pi$ interactions with the graphene surface, providing greater stability during functionalization steps. Regarding AO and FSC, its smaller π-conjugation suggests weaker surface interactions that limit stable attachment. The choice of solvent also significantly influenced the immobilization efficiency, with DMF facilitating the highest pDNA surface density. As a polar aprotic solvent, DMF enhances the solubility and distribution of PBSE, inducing a stable attachment to the graphene surface, optimizing interaction, and minimizing interlinker repulsion. In contrast, the other two solvents used limited linker solubility, resulting in lower effective coverage, possibly due to partial aggregation or reduced linker mobility.

Figure 2 data were also fitted with the logistic function to quantitatively assess the binding kinetics of pDNA adsorption, Figure S7. The fitting provides several parameters with p indicating the steepness of the sigmoidal curve in the function, Table S1. According to Figure 2, the linkers dissolved in DMF exhibit a significant frequency shift approximately 150 s after introducing the pDNA, with p values above 4, a change not consistently observed with the other solvents. This reflects the fast-binding transition when pDNA flows through the QCM-D chamber. Additionally, DMF as the dissolution solvent consistently resulted in the highest probe immobilization signal across all cases, Δf of approximately -9.11 ± 0.31 Hz, Figure 2A–C. In contrast, DMSO and the EtOH-DMF showed a slower increase in frequency, with p values between 1.7 and 3.2, indicating a more gradual pDNA binding and the lowest pDNA immobilization, Figure 2D–I.

Both AO and FSC linkers in 10% DMF in EtOH mixture, behaved slightly differently with p values of 3.8 and 2.6, respectively, as well as AO in DMSO, p values of 3.2, indicating faster kinetics and displaying high pDNA adsorption rate, $\Delta f \sim -6$ Hz, Figure 2H–I. In summary, the solvent that provided slower kinetics for pDNA binding was the DMSO, followed by 10% EtOH/DMF, while the fastest binding was observed with DMF. The desorption rate followed a similar trend for all linkers and solvents, except for AO in 10% DMF in EtOH, which showed a noticeably faster desorption rate (Figure 2I). Interestingly, this condition also exhibited one of the fastest adsorption rates, suggesting that AO might have reduced solubility in this solvent mixture, leading to weaker surface interactions and less stable adsorption. Moreover, it is also possible that the lower solvation ability of this solvent mixture may contribute to undissolved residues, possibly leading to nonspecific adsorption. It should be noted that the observed molecular density during functionalization represents an

https://doi.org/10.1021/acs.langmuir.4c03420
Langmuir 2025, 41, 263–273

equilibrium value achieved with a saturating concentration of pDNA. Some pDNA molecules are expected to diffuse into the active linker occasionally and, upon unsuccessful binding attempts, subsequently move away from the surface. The desorption rate followed a similar trend for all linkers and solvents, except for AO in 10% DMF in EtOH, which showed a noticeably faster desorption rate (Figure 2I).

Overall, the highest density of pDNA immobilized on the modified graphene surface was achieved with PBSE dissolved in DMF, reaching $1.27 \pm 0.04 \times 10^{13}$ molecules/cm^2 of DNA. This result aligns with our previous findings[37] and represents one of the fastest binding rates observed.

Table 2 presents theoretical and observed surface density data for the 3 linkers. Molecular footprints for the three linkers were obtained using ACD chemSketch software, assuming a planar face-to-face binding linker/graphene modulated as an elliptical area to reflect the different possible directional attachments of the linkers. The obtained footprint is larger than the area of the fused benzene rings to account for the necessary interatomic space between consecutive molecules, even assuming perfect coverage. PBSE, with its 4 fused benzene rings, and AO, with 3 fused rings, have closely resembled footprints, whereas FSC, with one 5-carbon ring sided by two benzene rings, is 1.5-fold smaller. In this work, we could not perform the linker functionalization step under QCM-D monitoring due to the incompatibility between the solvents used and the plastic tubing of the QCM-D equipment. Therefore, the measured linker densities are indirect measurements from two successive steps: the actual linker immobilization density and the linker-pDNA reaction. Linker footprints are more significant when compared with the 1.13 nm^2 of ssDNA (cross-sectional radius of 0.6 nm[42]), modeled as a circular area. Therefore, in the case of a linker stacked face-to-face on graphene, pDNA density is mainly ruled by the spatial distribution of the linker molecules on the surface. The effective coverage, obtained from the ratio of measured pDNA and theoretical surface densities of the linker, suggests values ranging from 15% to 25%.

An immediate conclusion is that the linker is far from fully covering the available surface area, even though a relatively high concentration of 10 mM was used for the functionalization step. One explanation could be that the bidimensional molecular distribution, due to the random nature of the linker diffusion and sedimentation toward the graphene surface, resulted in random packing, which is loose compared to the regular tessellation of the linker footprints that define the densest plane. However, against this argument, mathematical approaches to the random packing problem have shown that the 2D random packing is only slightly lower than the densest plane by a small percentage.[60,61]

Regarding intermolecular spacing, the distance between linkers, as deduced from the densest distribution and the measured density, assuming a homogeneous linker distribution, differs roughly by a factor of 2, from 2.1 to 4.2 nm in the case of PBSE, Table 2. Because the linker densities are indirect measurements, the lower observed coverage may relate more to the linker-pDNA reaction than the linker density. Electrostatic repulsion between 25-mer ssDNA (~8 nm) molecules cannot be neglected with the calculated intermolecular distances. They may reduce the ability of the DNA molecules to bind to the linker even when linker molecules are available, resulting in a lower pDNA density than the underlying linker density. Additionally, this effect may contribute to the number of unreacted linker molecules, which are prevented from reacting with pDNA due to nearby, already reacted, linker-pDNA complexes. Our observations of DNA desorption and unspecifically bound groups could also partially result from linker or linker-pDNA configurations that were unstable throughout the functionalization process and desorbed during buffer recirculation.

When comparing the density of functionalization obtained with the three linkers, we observed that the density of pDNA increases with the linker footprint. This observation contradicts the intuitive rationale that a smaller linker footprint would allow denser packing on the surface. In addition to the above arguments, one contributing factor to the final lower density with a smaller linker footprint is the presumably reduced interaction energy with graphene associated with linkers with fewer benzene rings. This reduced interaction energy is due to less extensive face-to-face surface contact and decreased electron cloud overlap, leading to weaker attachment of these linkers. As a result, poorly attached groups may be washed away during the functionalization step, contributing to the overall lower density.

Interestingly, a study by Hinnemo et al. on Pyrene-butyric acid (PBA) coverage on graphene[62] found that vertical stacking of the benzene rings becomes energetically favorable as the linker concentration increases, reaching its maximum at 10 mM, the same concentration used in this work. This stacking configuration could theoretically enhance the surface coverage by facilitating closer packing of the linkers. However, when comparing our pDNA surface coverage using PBSE with those reported in the literature ($\approx 1 \times 10^{11}$ molecules/cm^2, Table S2), our results demonstrate a surface coverage enhanced by 2 orders of magnitude.[41,44] One could consider that such a higher functionalization coverage could require upright conformation, increasing the chance of pDNA to move close to the surface and to react with active linker's succinimide groups, which is likely the primary reason for the obtained higher surface coverage. However, with an average coverage ratio below 25%, the vertical stacking would only be possible through a patchwork functionalization with areas of very high linker density and areas without linker molecules, a hypothesis for which there is no evidence, and is not supported by our previous work.[63]

The high surface coverage also results from the surface characteristics of the graphene layer. Surface topography dominates over probe density to enhance hybridization in nanostructured materials.[64] However, graphene is planar. Efforts were made to reduce graphene nucleation sites during graphene growth, leading to crystal sizes of tens or hundreds of micrometers, and improving the cleanliness of chemical residues during the graphene process.[65] With a cleaner surface, a more significant proportion of the surface is available for functionalization. The cleanliness of graphene surfaces cannot reach the same levels as that of gold thin-film surfaces, where plasma cleaning to strip all organics is very efficient. Nevertheless, the functionalization densities were comparable to the reference DNA immobilization on gold (oligo ≈20 mer), whether using a single-point thiol-based attachment or an attachment via ligands with a consistent footprint.[66]

The pDNA immobilization followed a kinetic rate as fast as the trend observed for gold−thiol DNA, up to 15 min. Therefore, the kinetics of graphene-linker ssDNA immobilization is not a limitation. The linker most commonly used in practice—PBSE—produced the highest surface densities of

https://doi.org/10.1021/acs.langmuir.4c03420
Langmuir 2025, 41, 263−273

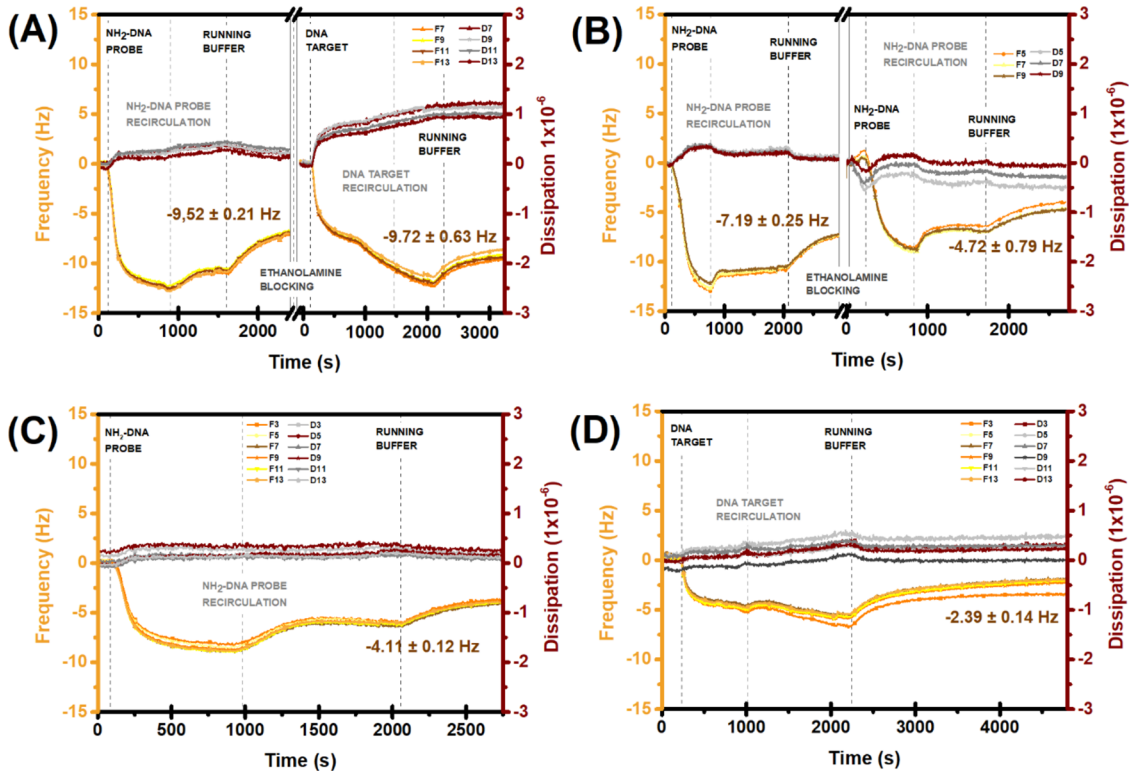


Figure 3. QCM-D frequency (orange, left axis) and dissipation (brown, right axis) change vs time response of DNA hybridization experiments. (A) PBSE/pDNA/ETA/tDNA and three controls: (B) control (i) PBSE/pDNA/ETA/pDNA, (C) control (ii) PBSE/ETA/pDNA and (D) control (iii) PBSE/ETA/tDNA. The time break visible in (A, B) corresponds to the application of ETA outside the QCM chamber. The frequency value in the graphs corresponds to Δf (Hz) between the baseline before the probe's introduction and the baseline acquisition's end.

DNA probes with the different solvents, reinforcing its suitability in biosensing applications.

DNA Hybridization Experiments. Our findings provide evidence that the interplay between the surface, the linkers' aromatic ligands, solvent quality, and concentrations is crucial in determining the effectiveness of these linkers to functionalize graphene for subsequent pDNA attachment, however, the DNA hybridization needed to be assessed. Thus, the QCM-D hybridization experiments were performed using PBSE dissolved in DMF.

Figure 3A (left) showed a fast shift to a stable frequency around 11 Hz upon introducing pDNA, resulting in a final frequency shift of −9.52 ± 0.21 Hz (Figure 3A). Afterward, the sample was removed from the QCM-D chamber (time-axis break in Figure 3A), and the unreacted activated ester ligands were blocked with ethanolamine. The sample was then reintroduced in the chamber and exposed to the complementary sequence of tDNA (vertical dashed line at t = 150 s for hybridization). The QCM signal after injection and recirculation of the tDNA is shown in Figure 3A (right), with the general kinetics profile similar to the one observed for the immobilization of pDNA. The Δf reaches the value of −9.72 ± 0.63 Hz, corresponding to a tDNA density of 1.39 ± 0.09 × 10^{13} molecules/cm^2, which is higher than the surface coverage estimation for pDNA of 1.31 ± 0.03 × 10^{13}. This slightly higher surface density for tDNA vs pDNA suggests that a small fraction of the tDNA is bound nonspecifically rather than in a hybrid form on the surface. This nonspecific contribution was further quantified through three additional experiments: (i) PBSE/pDNA/ETA/pDNA to verify the binding capacity of pDNA in a second interaction after ethanolamine blocking (Figure 3B); (ii) PBSE/ETA/pDNA to study the ability of pDNA to bind onto a surface of a putative entirely blocked PBSE (Figure 3C); and (iii) PBSE/ETA/tDNA to study the capability of tDNA binding onto a surface of a putative entirely blocked PBSE (Figure 3D).

In the first of the additional experiments, denoted as (i) (Figure 3B), the graphene surface functionalized with PBSE tethered pDNA similarly to the previous experiment (cf. Figure 3B, left and Figure 3A, left), leading to a rapid and consistent shift in resonance frequency of −7.19 Hz. After ethanolamine blocking of the NHS reactive ester, one would expect that adding more pDNA would not lead to a higher signal because all reacting sites were already occupied by pDNA or blocked with ETA. However, the second round of pDNA resulted in a shift in resonance frequency of −4.72 Hz (Figure 3B, right), corresponding to an additional density of 6.6 ± 0.5 × 10^{12} molecules/cm^2. This increase may include two contributions, one from nonspecific interactions between pDNA and the graphene surface and one from a reaction with activated ester that did not previously react with ethanolamine.

Controls (ii) PBSE/ETA/pDNA (Figure 3C) and (iii) PBSE/ETA/tDNA (Figure 3D) consisted of reacting the activated NHS reactive ester groups of PBSE on the surface with ethanolamine, followed by an attempt to adsorb DNA on the surface. In control (ii), pDNA is used, and the experiment results are similar to control (i), with a decrease in frequency of −4.11 Hz. Control (iii) consists of the same as experiment (ii) using tDNA instead of pDNA, resulting in a reduction in frequency of −2.39 Hz, indicating that a fraction of the DNA strands from solution adsorbs onto the surface.

https://doi.org/10.1021/acs.langmuir.4c03420
Langmuir 2025, 41, 263−273

In the three controls, ethanolamine in excess should completely react with the activated ester groups into an amide formation, preventing further specific interactions between NHS and the amine-modified pDNA. However, in controls (i) and (ii) after ETA exposure, pDNA may still react with any remaining nonblocked esters or adsorb nonspecifically onto the graphene surface. The similar results observed in both controls indicate that the layer of pDNA added onto PBSE does not introduce significant steric hindrance, allowing additional pDNA to bind onto the surface. In control (iii), tDNA, which is not amine-modified, cannot react with NHS and can only interact through nonspecific adsorption onto the graphene surface. As a result, it produces a notably lower change in frequency compared to control (ii), where pDNA had two potential interaction pathways.

Quantitatively, control (iii) provides a nonspecific DNA binding onto the graphene-PBSE-ETA surface of $3.3 \pm 0.7 \times 10^{12}$ molecules/cm^2. The difference between experiments (iii) and (ii) provides the amount of pDNA still able to bind to unreacted PBSE after ETA, of $2.4 \pm 0.7 \times 10^{12}$ molecules/cm^2. When referring these numbers to the density of functionalization on the surface from Table 1 (PBSE/DMF), they correspond to an additional nonspecific binding of approximately 26% DNA that may interact with the surface and an unreacted portion of PBSE after the ETA step of 19%, leading to an efficiency of the PBSE-ETA reaction estimated to be approximately 80%. These results highlight the robustness of the functionalization process but even more remarkable is the high hybridization efficiency implied by capturing the estimated $1.39 \pm 0.09 \times 10^{13}$ molecules/cm^2 of tDNAs onto a surface with $1.31 \pm 0.03 \times 10^{13}$ molecules/cm^2 density of DNA probes. Even accounting for up to ca. 25% of targets that become adsorbed nonspecifically, the implied hybridization efficiency around 71% is high for this range of probe density.[51,64] Although not evaluated here, PEG could help minimize nonspecific DNA adsorption on the graphene surface.[42]

In summary, the choice of the linker and the respective solvent impacted the final pDNA density similarly. The solvent inducing the best performance was the DMF, with a probe density 30% higher than that obtained with 10%DMF/EtOH. This observation is consistent with the effect of linker orientation, considering that the solvent plays an important role when minimizing repulsion between the linker and graphene or between nearby molecules. Additionally, increasing the linker footprint increases the distance between successive pDNA that react with the linker, minimizing repulsive interactions between the charged pDNA strands approaching the binding sites.

Our results suggest electrostatics, space constraints, and accessibility primarily governed hybridization.

CONCLUSIONS

In this study, we used graphene field-effect transistor-based biosensing chips and quartz crystal microbalance with dissipation (QCM-D) measurements for the real-time monitoring of immobilization of DNA probes and DNA hybridization as a function of pairing heterobifunctional linkers (PBSE, FSC, and AO) and solvents (DMF, DMSO, 10% DMF in EtOH) for the initial noncovalent functionalization of single-layer graphene surfaces. The highest density of the immobilized DNA probes was achieved for graphene surfaces functionalized with PBSE in DMF. The high density of pDNA is achievable via a two-step biofunctionalization leading to $1.27 \pm 0.04 \times 10^{13}$ molecules/cm^2 of pDNA, corresponding to a surface packing density of 25%. The functionalization density was affected by an energetically favorable effect of a larger linker footprint and a reduced steric and electrostatic hindrance between DNA molecules associated with a larger footprint. The quality of the solvent and its effect on attenuating molecule repulsion strongly affect the probe density.

Out of the total DNA adsorbed onto the surface during DNA circulation, about 30% is desorbed after the QCM rinsing step with running buffer, corresponding to weekly attached DNA. The remaining immobilized DNA can further be analyzed as specific and nonspecifically bound, where up to 26% of DNA can bind nonspecifically onto the graphene surface. The blocking of the unreacted NHS groups of the linker, using ethanolamine, was measured to have an efficiency of about 80%. The hybridization efficiency of pDNA immobilized on graphene with complementary tDNA was 70%.

ASSOCIATED CONTENT

Supporting Information

The Supporting Information is available free of charge at https://pubs.acs.org/doi/10.1021/acs.langmuir.4c03420.

Details on graphene growth and characterization; graphene transfer; and verification of the QCM crystal; description of pDNA immobilization with PBSE in DMF; the calculations for estimating surface density using the Sauerbrey model; the kinetic results; and a survey of strategies for surface-immobilized DNA layers for comparison (PDF)

AUTHOR INFORMATION

Corresponding Authors

Jérôme Borme − *International Iberian Nanotechnology Laboratory, 4715-330 Braga, Portugal;* orcid.org/0000-0002-5622-7760; Email: jerome.borme@inl.int

Joana Rafaela Guerreiro − *International Iberian Nanotechnology Laboratory, 4715-330 Braga, Portugal; CIETI-LabRISE, School of Engineering, Polytechnic of Porto, 4200-072 Porto, Portugal; CEB—Centre of Biological Engineering, University of Minho, 4710-057 Braga, Portugal;* orcid.org/0000-0001-8719-1978; Email: joanarlguerreiro@gmail.com, jrg@isep.ipp.com

Authors

Telma Domingues − *International Iberian Nanotechnology Laboratory, 4715-330 Braga, Portugal; Center of Physics of the Universities of Minho and Porto, University of Minho, 4710-057 Braga, Portugal*

Chun-Da Liao − *International Iberian Nanotechnology Laboratory, 4715-330 Braga, Portugal*

Marta Prado − *International Iberian Nanotechnology Laboratory, 4715-330 Braga, Portugal; LHICA Department of Analytical Chemistry, Nutrition and Bromatology, Campus Terra, University of Santiago de Compostela (USC), 27002 Lugo, Spain*

M. Fátima Cerqueira − *International Iberian Nanotechnology Laboratory, 4715-330 Braga, Portugal; Center of Physics of the Universities of Minho and Porto, University of Minho, 4710-057 Braga, Portugal*

Dmitri Y. Petrovykh − *International Iberian Nanotechnology Laboratory, 4715-330 Braga, Portugal;* orcid.org/0000-0001-9089-4076

Pedro Alpuim − *International Iberian Nanotechnology Laboratory, 4715-330 Braga, Portugal; Center of Physics of the Universities of Minho and Porto, University of Minho, 4710-057 Braga, Portugal*

Complete contact information is available at: https://pubs.acs.org/10.1021/acs.langmuir.4c03420

Author Contributions

Conceptualization, methodology, resources: J.R.L.G., J.B., M.P., and P.A.; T.D. and C.D.L. carried out graphene growth and transfer, graphene characterization was performed by M.F.C., and QCM-D measurements were performed by T.D. and J.R.L.G.; Writing—original draft: T.D.; Figures preparation: T.D., M.F.C., J.R.L.G.; Project administration: P.A. and M.P.; Writing—review and editing: M.F.C., D.Y.P., M.P., J.B., J.R.L.G., and P.A. All authors have approved the final version of the manuscript.

Notes

The authors declare no competing financial interest.

■ ACKNOWLEDGMENTS

We acknowledge the partial support by the Portuguese Foundation for Science and Technology (FCT) in the framework of Project POCI-01-0145-FEDER-031069 (PORTGRAPHE) and UIDP//04650//2020. One of the authors (T.D.) acknowledges FCT for the SFRH/BD/08181/2020 grant. The author J.RL.G. acknowledges FCT for the 2020.02120.CEECIND grant.

■ REFERENCES

(1) Zeng, R.; Wang, W.; Cai, G.; Huang, Z.; Tao, J.; Tang, D.; Zhu, C. Single-Atom Platinum Nanocatalyst-Improved Catalytic Efficiency with Enzyme-DNA Supermolecular Architectures. *Nano Energy* **2020**, *74*, 104931−104939.

(2) Lv, S.; Zhang, K.; Zhu, L.; Tang, D. Zif-8-Assisted Nayf4:Yb,Tm@zno Converter with Exonuclease Iii-Powered DNA Walker for Near-Infrared Light Responsive Biosensor. *Anal. Chem.* **2020**, *92* (1), 1470−1476.

(3) Yu, M.; He, T.; Wang, Q.; Cui, C. Unraveling the Possibilities: Recent Progress in DNA Biosensing. *Biosensors* **2023**, *13* (9), 889−917.

(4) Rao, A. N.; Grainger, D. W. Biophysical Properties of Nucleic Acids at Surfaces Relevant to Microarray Performance. *Biomater. Sci.* **2014**, *2* (4), 436−471.

(5) Zeng, R.; Gong, H.; Li, Y.; Li, Y.; Lin, W.; Tang, D.; Knopp, D. CRISPR-Cas12a-Derived Photoelectrochemical Biosensor for Point-of-Care Diagnosis of Nucleic Acid. *Anal. Chem.* **2022**, *94* (20), 7442−7448.

(6) Gong, H.; Wu, Y.; Zeng, R.; Zeng, Y.; Liu, X.; Tang, D. CRISPR/Cas12a-Mediated Liposome-Amplified Strategy for the Photoelectrochemical Detection of Nucleic Acid. *Chem. Commun.* **2021**, *57* (71), 8977−8980.

(7) Hua, Y.; Ma, J.; Li, D.; Wang, R. DNA-Based Biosensors for the Biochemical Analysis: A Review. *Biosensors* **2022**, *12* (3), 183−205.

(8) Mondal, H. S.; Feng, Y.; Biswas, G.; Hossain, M. Z. Applications and Challenges of DNA-Based Electrochemical Biosensors for Monitoring Health: A Systematic Review. *DNA* **2024**, *4* (3), 300−317.

(9) Asefifeyzabadi, N.; Das, P. K.; Onorimuo, A. H.; Durocher, G.; Shamsi, M. H. DNA Interfaces with Dimensional Materials for Biomedical Applications. *RSC Adv.* **2021**, *11* (45), 28332−28341.

(10) Abu-Salah, K. M.; Zourob, M. M.; Mouffouk, F.; Alrokayan, S. A.; Alaamery, M. A.; Ansari, A. A. DNA-Based Nanobiosensors as an Emerging Platform for Detection of Disease. *Sensors* **2015**, *15* (6), 14539−14568.

(11) Sun, S.; Chen, J. Recent Advances in Hydrogel-Based Biosensors for Cancer Detection. *ACS Appl. Mater. Interfaces* **2024**, *16* (36), 46988−47002.

(12) Wang, Q.; Wang, J.; Huang, Y.; Du, Y.; Zhang, Y.; Cui, Y.; Kong, D. M. Development of the DNA-Based Biosensors for High Performance in Detection of Molecular Biomarkers: More Rapid, Sensitive, and Universal. *Biosens. Bioelectron.* **2022**, *197*, 113739−113746.

(13) Chu, M.; Zhang, Y.; Ji, C.; Zhang, Y.; Yuan, Q.; Tan, J. DNA Nanomaterial-Based Electrochemical Biosensors for Clinical Diagnosis. *ACS Nano* **2024**, *18* (46), 31713−31736.

(14) Hwu, S.; Garzuel, M.; Forró, C.; Ihle, S. J.; Reichmuth, A. M.; Kurdzesau, F.; Vörös, J. An Analytical Method to Control the Surface Density and Stability of DNA-Gold Nanoparticles for an Optimized Biosensor. *Colloids Surf., B* **2020**, *187*, 110650−110658.

(15) Rashid, J. I. A.; Yusof, N. A. The Strategies of DNA Immobilization and Hybridization Detection Mechanism in the Construction of Electrochemical DNA Sensor: A Review. *Sens. Bio-Sens. Res.* **2017**, *16*, 19−31.

(16) Monserud, J. H.; Schwartz, D. K. Mechanisms of Surface-Mediated DNA Hybridization. *ACS Nano* **2014**, *8* (5), 4488−4499.

(17) Veselinovic, J.; Almashtoub, S.; Seker, E. Anomalous Trends in Nucleic Acid-Based Electrochemical Biosensors with Nanoporous Gold Electrodes. *Anal. Chem.* **2019**, *91* (18), 11923−11931.

(18) Das, P.; Zafar, S. Mechanistic Influence of Nanometer Length-Scale Surface Chemistry on DNA Hybridization. *ACS Nano* **2015**, *9* (7), 7466−7478.

(19) Vericat, C.; Vela, M. E.; Benitez, G.; Carro, P.; Salvarezza, R. C. Self-Assembled Monolayers of Thiols and Dithiols on Gold: New Challenges for a Well-Known System. *Chem. Soc. Rev.* **2010**, *39* (5), 1805−1834.

(20) Dilimon, V. S.; Rajalingam, S.; Delhalle, J.; Mekhalif, Z. Self-Assembly Mechanism of Thiol, Dithiol, Dithiocarboxylic Acid, Disulfide and Diselenide on Gold: An Electrochemical Impedance Study. *Phys. Chem. Chem. Phys.* **2013**, *15* (39), 16648−16656.

(21) Gong, H.; Hu, X.; Zeng, R.; Li, Y.; Xu, J.; Li, M.; Tang, D. CRISPR/Cas12a-Based Photoelectrochemical Sensing of MicroRNA on Reduced Graphene Oxide-Anchored Bi2WO6 Coupling with Catalytic Hairpin Assembly. *Sens. Actuators, B* **2022**, *369*, 132307−132314.

(22) Cai, G.; Yu, Z.; Ren, R.; Tang, D. Exciton-Plasmon Interaction between AuNPs/Graphene Nanohybrids and CdS Quantum Dots/TiO2 for Photoelectrochemical Aptasensing of Prostate-Specific Antigen. *ACS Sens.* **2018**, *3* (3), 632−639.

(23) Sang, M.; Shin, J.; Kim, K.; Yu, K. J. Electronic and Thermal Properties of Graphene and Recent Advances in Graphene Based Electronics Applications. *Nanomaterials* **2019**, *9* (3), 374−407.

(24) Ohno, Y.; Okamoto, S.; Maehashi, K.; Matsumoto, K. Direct Electrical Detection of DNA Hybridization Based on Electrolyte-Gated Graphene Field-Effect Transistor. *Jpn. J. Appl. Phys.* **2013**, *52* (11), 110107−110110.

(25) Suvarnaphaet, P.; Pechprasarn, S. Graphene-Based Materials for Biosensors: A Review. *Sensors* **2017**, *17* (10), 2161−2185.

(26) Kamali, A. R. Eco-Friendly Production of High Quality Low Cost Graphene and its Application in Lithium Ion Batteries. *Green Chem.* **2016**, *18* (7), 1952−1964.

(27) Ping, J.; Vishnubhotla, R.; Vrudhula, A.; Johnson, A. T. C. Scalable Production of High-Sensitivity, Label-Free DNA Biosensors Based on Back-Gated Graphene Field Effect Transistors. *ACS Nano* **2016**, *10* (9), 8700−8704.

(28) Pumera, M. Graphene in Biosensing. *Mater. Today* **2011**, *14* (7), 308−315.

(29) Wu, X.; Mu, F.; Wang, Y.; Zhao, H. Graphene and Graphene-Based Nanomaterials for DNA Detection: A Review. *Molecules* **2018**, *23* (8), 2050−2073.

(30) Peña-Bahamonde, J.; Nguyen, H. N.; Fanourakis, S. K.; Rodrigues, D. F. Recent Advances in Graphene-Based Biosensor Technology with Applications in Life Sciences. *J. Nanobiotechnol.* **2018**, *16* (1), 75−92.
(31) Wang, X.; Shi, G. An Introduction to the Chemistry of Graphene. *Phys. Chem. Chem. Phys.* **2015**, *17* (43), 28484−28504.
(32) Bueno, R. A.; Martínez, J. I.; Luccas, R. F.; Del Árbol, N. R.; Munuera, C.; Palacio, I.; Palomares, F. J.; Lauwaet, K.; Thakur, S.; Baranowski, J. M.; Strupinski, W.; López, M. F.; Mompean, F.; García-Hernández, M.; Martín-Gago, J. A. Highly Selective Covalent Organic Functionalization of Epitaxial Graphene. *Nat. Commun.* **2017**, *8*, No. 15306.
(33) Krishnan, S. K.; Singh, E.; Singh, P.; Meyyappan, M.; Nalwa, H. S. A Review on Graphene-Based Nanocomposites for Electrochemical and Fluorescent Biosensors. *RSC Adv.* **2019**, *9* (16), 8778−8781.
(34) Narayan, J.; Bezborah, K. Recent Advances in the Functionalization, Substitutional Doping and Applications of Graphene/Graphene Composite Nanomaterials. *RSC Adv.* **2024**, *14* (19), 13413−13444.
(35) Palacio, I.; Moreno, M.; Náñez, A.; Purwidyantri, A.; Domingues, T.; Cabral, P. D.; Borme, J.; Marciello, M.; Mendieta-Moreno, J. I.; Torres-Vázquez, B.; Martínez, J. I.; López, M. F.; García-Hernández, M.; Vázquez, L.; Jelínek, P.; Alpuim, P.; Briones, C.; Martín-Gago, J. Á. Attomolar Detection of Hepatitis C Virus Core Protein Powered by Molecular Antenna-like Effect in a Graphene Field-Effect Aptasensor. *Biosens. Bioelectron.* **2023**, *222*, 115006−115013.
(36) Kushalkar, M. P.; Liu, B.; Liu, J. Promoting DNA Adsorption by Acids and Polyvalent Cations: Beyond Charge Screening. *Langmuir* **2020**, *36* (38), 11183−11195.
(37) Mensah, K.; Cissé, I.; Pierret, A.; Rosticher, M.; Palomo, J.; Morfin, P.; Plaçais, B.; Bockelmann, U. DNA Hybridization Measured with Graphene Transistor Arrays. *Adv. Healthcare Mater.* **2020**, *9* (16), No. 2000260.
(38) Li, B.; Ou, P.; Wei, Y.; Zhang, X.; Song, J. Polycyclic Aromatic Hydrocarbons Adsorption onto Graphene: A DFT and AIMD Study. *Materials* **2018**, *11* (5), 726−740.
(39) Gao, Z.; Xia, H.; Zauberman, J.; Tomaiuolo, M.; Ping, J.; Zhang, Q.; Ducos, P.; Ye, H.; Wang, S.; Yang, X.; Lubna, F.; Luo, Z.; Ren, L.; Johnson, A. T. C. Detection of Sub-fM DNA with Target Recycling and Self-Assembly Amplification on Graphene Field-Effect Biosensors. *Nano Lett.* **2018**, *18* (6), 3509−3515.
(40) Huang, Z.; Liu, J. Length-Dependent Diblock DNA with Poly-Cytosine (Poly-C) as High-Affinity Anchors on Graphene Oxide. *Langmuir* **2018**, *34* (3), 1171−1177.
(41) Tang, L.; Wang, Y.; Li, J. The Graphene/Nucleic Acid Nanobiointerface. *Chem. Soc. Rev.* **2015**, *44* (19), 6954−6980.
(42) Varghese, N.; Mogera, U.; Govindaraj, A.; Das, A.; Maiti, P. K.; Sood, A. K.; Rao, C. N. R. Binding of DNA Nucleobases and Nucleosides with Graphene. *ChemPhysChem* **2009**, *10* (1), 206−210.
(43) Lu, C.; Huang, Z.; Liu, B.; Liu, Y.; Ying, Y.; Liu, J. Poly-Cytosine DNA as a High-Affinity Ligand for Inorganic Nanomaterials. *Angew. Chem.* **2017**, *129* (22), 6304−6308.
(44) Xu, S.; Zhan, J.; Man, B.; Jiang, S.; Yue, W.; Gao, S.; Guo, C.; Liu, H.; Li, Z.; Wang, J.; Zhou, Y. Real-Time Reliable Determination of Binding Kinetics of DNA Hybridization Using a Multi-Channel Graphene Biosensor. *Nat. Commun.* **2017**, *8*, 14902−14912.
(45) Campos, R.; Borme, J.; Guerreiro, J. R.; Machado, G.; Cerqueira, M. F.; Petrovykh, D. Y.; Alpuim, P. Attomolar Label-Free Detection of DNA Hybridization with Electrolyte-Gated Graphene Field-Effect Transistors. *ACS Sens.* **2019**, *4* (2), 286−293.
(46) Mishyn, V.; Hugo, A.; Rodrigues, T.; Aspermair, P.; Happy, H.; Marques, L.; Hurot, C.; Othmen, R.; Bouchiat, V.; Boukherroub, R.; Knoll, W.; Szunerits, S. The Holy Grail of Pyrene-Based Surface Ligands on the Sensitivity of Graphene-Based Field Effect Transistors. *Sens. Diagn.* **2022**, *1* (2), 235−244.
(47) Zhang, Z.; Luo, L.; Chen, G.; Ding, Y.; Deng, D.; Fan, C. Tryptamine Functionalized Reduced Graphene Oxide for Label-Free DNA Impedimetric Biosensing. *Biosens. Bioelectron.* **2014**, *60*, 161−166.
(48) Wang, L.; Qi, W.; Su, R.; He, Z. Noncovalent Functionalization of Graphene by CdS Nanohybrids for Electrochemical Applications. *Thin Solid Films* **2014**, *568* (1), 58−62.
(49) Ohno, Y.; Maehashi, K.; Inoue, K.; Matsumoto, K. Label-Free Aptamer-Based Immunoglobulin Sensors Using Graphene Field-Effect Transistors. *Jpn. J. Appl. Phys.* **2011**, *50*, 70120−70124.
(50) Prats-Alfonso, E.; Aviñó, A.; Guimerà, A.; Masvidal, E.; Illa, X.; Rius, G.; Eritja, R.; Garrido, J. A.; Villa, R. Label-Free Direct Detection of Thrombin through Graphene SGFET with Chemically Modified Aptamers, Graphene Conference, Dresden (Germany). 2018, 1.
(51) Xue, T.; Cui, X.; Guan, W.; Wang, Q.; Liu, C.; Wang, H.; Qi, K.; Singh, D. J.; Zheng, W. Surface Plasmon Resonance Technique for Directly Probing the Interaction of DNA and Graphene Oxide and Ultra-Sensitive Biosensing. *Biosens. Bioelectron.* **2014**, *58*, 374−379.
(52) Williamson, P.; Ijäs, H.; Shen, B.; Corrigan, D. K.; Linko, V. Probing the Conformational States of a PH-Sensitive DNA Origami Zipper via Label-Free Electrochemical Methods. *Langmuir* **2021**, *37* (25), 7801−7809.
(53) Gillissen, J. J. J.; Jackman, J. A.; Tabaei, S. R.; Cho, N. J. A Numerical Study on the Effect of Particle Surface Coverage on the Quartz Crystal Microbalance Response. *Anal. Chem.* **2018**, *90* (3), 2238−2245.
(54) Movilli, J.; Kolkman, R. W.; Rozzi, A.; Corradini, R.; Segerink, L. I.; Huskens, J. Increasing the Sensitivity of Electrochemical DNA Detection by a Micropillar-Structured Biosensing Surface. *Langmuir* **2020**, *36* (16), 4272−4279.
(55) No, Y. S.; Choi, H. K.; Kim, J. S.; Kim, H.; Yu, Y. J.; Choi, C. G.; Choi, J. S. Layer Number Identification of CVD-Grown Multilayer Graphene Using Si Peak Analysis. *Sci. Rep.* **2018**, *88*, 571−580.
(56) Inam, F.; Yan, H.; Reece, M. J.; Peijs, T. Dimethylformamide: An Effective Dispersant for Making Ceramic-Carbon Nanotube Composites. *Nanotechnology* **2008**, *19* (19), 195710−195715.
(57) Pramanik, C.; Gissinger, J. R.; Kumar, S.; Heinz, H. Carbon Nanotube Dispersion in Solvents and Polymer Solutions: Mechanisms, Assembly, and Preferences. *ACS Nano* **2017**, *11* (12), 12805−12816.
(58) Chauhan, A. P. S.; Chawla, K. Comparative Studies on Graphite and Carbon Black Powders, and Their Dispersions. *J. Mol. Liq.* **2016**, *221*, 292−297.
(59) Fernandes, E.; Cabral, P. D.; Campos, R.; Machado, G.; Cerqueira, M. F.; Sousa, C.; Freitas, P. P.; Borme, J.; Petrovykh, D. Y.; Alpuim, P. Functionalization of Single-Layer Graphene for Immunoassays. *Appl. Surf. Sci.* **2019**, *480*, 709−716.
(60) Torquato, S.; Stillinger, F. H. Jammed Hard-Particle Packings: From Kepler to Bernal and Beyond. *Rev. Mod. Phys.* **2010**, *82* (3), 2633−2672.
(61) Zaccone, A. Explicit Analytical Solution for Random Close Packing in D = 2 and D = 3. *Phys. Rev. Lett.* **2022**, *128* (2), 28002−28006.
(62) Hinnemo, M.; Zhao, J.; Ahlberg, P.; Hägglund, C.; Djurberg, V.; Scheicher, R. H.; Zhang, S. L.; Zhang, Z.-B. On Monolayer Formation of Pyrenebutyric Acid on Graphene. *Langmuir* **2017**, *33* (15), 3588−3593.
(63) Adão, R. M. R.; Campos, R.; Figueiras, E.; Alpuim, P.; Nieder, J. B. Graphene Setting the Stage: Tracking DNA Hybridization with Nanoscale Resolution. *2D Mater.* **2019**, *6* (4), 45056−45067.
(64) Bin, X.; Sargent, E. H.; Kelley, S. O. Nanostructuring of Sensors Determines the Efficiency of Biomolecular Capture. *Anal. Chem.* **2010**, *82* (14), 5928−5931.
(65) Liao, C.-D.; Da; Capasso, A.; Queirós, T.; Domingues, T.; Cerqueira, F.; Nicoara, N.; Borme, J.; Freitas, P.; Alpuim, P. Optimizing PMMA Solutions to Suppress Contamination in the Transfer of CVD Graphene for Batch Production. *Beilstein J. Nanotechnol.* **2022**, *13*, 796−806.
(66) Schreiner, S. M.; Shudy, D. F.; Hatoh, A. L.; Opdahl, A.; Whitman, L. J.; Petrovykh, D. Y. Controlled and Efficient Hybrid-

https://doi.org/10.1021/acs.langmuir.4c03420
Langmuir 2025, 41, 263−273

ization Achieved with DNA Probes Immobilized Solely through Preferential DNA-Substrate Interactions. *Anal. Chem.* **2010**, *82* (7), 2803−2810.

https://doi.org/10.1021/acs.langmuir.4c03420
Langmuir 2025, 41, 263−273